





Controlling the generation of elliptically polarized isolated attosecond pulses from mixed gases with a polarization-gating technique

Chunyang Zhai ¹, Yifan Liu,¹ Xiang Li ¹, Xi Liu ², Fengrun Wu,¹ Shuaijie Kang,¹ Zhengfa Li,¹ Xinzhe Dong,³ Yingbin Li,^{1,*} Qingbin Tang,^{1,†} Xiaosong Zhu ⁴, and Benhai Yu¹

¹College of Physics and Electronic Engineering, *Xinyang Normal University*, Xinyang 464000, China

²School of Physics and New Energy, *Xuzhou University of Technology*, Xuzhou 221018, China

³School of New Energy Science and Technology, *Xinyang Institute of Technology*, *Xinyang Normal University*, Xinyang 465150, China

⁴Wuhan National Laboratory for Optoelectronics and School of Physics, *Huazhong University of Science and Technology*, Wuhan 430074, China



(Received 22 May 2024; revised 12 August 2024; accepted 20 August 2024; published 3 September 2024)

The generation of elliptically polarized attosecond pulses has become a crucial issue due to the growing interest in its application to probing circular dichroism and chirality in matter. Here, we propose a method capable of generating isolated attosecond pulses (IAPs) with near-circular polarization. Through the combination of the mixed gases scheme with a polarization gating laser field, we obtain an IAP with an ellipticity of 0.91 and a pulse duration of 290 as. Our analysis indicates that the polarization of attosecond pulses is predominantly influenced by the mixed gases, specifically by the selective interference between the recombination dipole moments of different gas components. In contrast to polarization, the temporal profile of attosecond pulses mainly depends on the laser field. Our approach achieves independent control of the polarization and temporal properties of IAPs by adjusting the gas mixture and the polarization gating laser field, respectively, thus paving an effective and convenient way to generate and control elliptically polarized IAPs.

DOI: [10.1103/PhysRevA.110.033507](https://doi.org/10.1103/PhysRevA.110.033507)

I. INTRODUCTION

High-order harmonic generation (HHG) is a nonlinear phenomenon that occurs during the interaction between intense laser fields and various forms of matter, including atoms, molecules, liquids, and solids [1–7]. The underlying physical picture of the atomic or molecular interaction process is well described by the semiclassical three-step model [8]. In the first step, an electron is ionized by the laser field. In the second step, the released electron is accelerated in the laser field. When the field reverses, the free electron is likely to return to the ion and recombine. In the final step, the recombination process converts the kinetic energy of the electron into emitted high-energy photons, i.e., high-order harmonic radiation that supports attosecond pulse trains or isolated attosecond pulses (IAPs) generation. Attosecond pulses have emerged as a powerful tool for probing electron dynamics in matter with unprecedented high temporal resolution [9–12]. In particular, circularly or elliptically polarized high-order harmonics and attosecond pulses have attracted significant interest owing to their unique ability to directly probe the ultrafast dynamics of chiral systems and magnetic materials [13–15]. Because the harmonic polarization depends on the dipole direction, which is directly linked to the driving laser polarization, it is natural to anticipate that the ellipticity of the harmonics can be controlled with the ellipticity of the driving laser field

[16]. However, the recombination probability, and therefore the harmonic generation efficiency, drops dramatically as the ellipticity of the driving laser field increases [17–19].

To obtain circularly or elliptically polarized attosecond pulses, a crucial issue is effectively generating circularly or elliptically polarized high-order harmonics with the same helicity in a broad spectral range. Several schemes have been developed for generating circularly or elliptically polarized high-order harmonics at present. These schemes can be generally divided into two categories: *ex situ* and *in situ* generation. The first relies on polarization conversion after the HHG process. This can be achieved through the polarization sensitivity of metal surfaces or introducing a delay between two individual, phase-locked, and orthogonally polarized harmonic sources [20–22]. However, this approach often results in either very low harmonic efficiency or very high demands on experimental accuracy. The second approach directly produces nonzero ellipticity during the HHG process using specific media or tailored laser fields. The intrinsic constraint of gaseous media purity, such as misaligned molecules or unstable current-carrying states [23–26], obstructs the achievement of significant ellipticity in high-order harmonics. In recent years, the generation of elliptically polarized harmonics in solids using circularly polarized laser pulses, as well as bicircular corotating or counterrotating laser pulses, has also been reported [27–29]. In addition, an alternative way to overcome these obstacles in gaseous media has also been developed based on the tailored electric fields, enabling the generation of elliptically and even circularly polarized high-order harmonics. Several schemes of tailored laser fields, including

*Contact author: liyingbin2008@163.com

†Contact author: qingbintang@xynu.edu.cn

bichromatic circularly polarized fields [30–39], orthogonally two-color fields [40–44], and noncollinear fields [45–49], are currently being studied theoretically and experimentally. While these tailored laser fields enable the generation of desired polarization for high-order harmonics and attosecond pulses, they also determine the temporal waveform of the attosecond pulses. Specifically, the generation of IAPs requires either a few-cycle laser field or a gating laser field [50–54]. Due to this interdependence, it is impossible to control the polarization and temporal profile of attosecond pulses independently.

In this work, we theoretically investigate the polarization properties of high-order harmonics and attosecond pulses by combining the gating laser field scheme with the mixed gases scheme. Utilizing a polarization gating laser field that has high degree of control freedom, we obtain a supercontinuum, during which process only one helicity has a dominant contribution to the supercontinuum generated by a mixture of Ar and N₂, resulting in the generation of an elliptically polarized IAP in the time domain. Through a detailed theoretical description using quantum orbital analysis, we uncover the origin of the nonzero ellipticity in high-order harmonics and attosecond pulses. This ellipticity arises from the selective interference between the recombination dipole moments of gases with opposite orbital parities. Therefore, the temporal profile and ellipticity of the attosecond pulses can be independently controlled by the laser field and the gas media, respectively.

II. NUMERICAL METHOD

In our calculation, the harmonic radiation is calculated based on the widely accepted Lewenstein model [55]. The validity of our approach has also been confirmed by numerically solving the time-dependent Schrödinger equation (TDSE). The induced dipole moment at time t can be expressed as follows [atomic units (a.u.) are used throughout unless otherwise stated]

$$D(t) = i \int_{-\infty}^t dt_i \left[\frac{\pi}{\xi + i(t - t_i)/2} \right]^{3/2} \mathbf{E}(t_i) \mathbf{d}[\mathbf{p}(t_i)] \times e^{-i[S(t_i, t) + I_p(t - t_i)]} \mathbf{d}^*[\mathbf{p}(t)] + \text{c.c.}, \quad (1)$$

where $\mathbf{E}(t)$ represents a time-dependent intense laser field, t_i denotes the time of ionization, I_p is the ionization potential of the target, $S(t_i, t)$ is the quasiclassical action, which is written as

$$S(t_i, t) = \int_{t_i}^t \frac{[\mathbf{p}_{\text{st}}(t_i, t) - \mathbf{A}(t')]^2}{2} dt', \quad (2)$$

where $\mathbf{A}(t) = -\int_{-\infty}^t \mathbf{E}(t') dt'$ is the vector potential of the laser field, and $\mathbf{p}_{\text{st}}(t_i, t) = \frac{1}{t - t_i} \int_{t_i}^t \mathbf{A}(t') dt'$ is the stationary momentum. $\mathbf{d}[\mathbf{p}(t_i)]$ and $\mathbf{d}^*[\mathbf{p}(t)]$ are the transition dipole moments and are defined as

$$\mathbf{d}[\mathbf{p}(t_i)] = \langle \mathbf{p}_{\text{st}} - \mathbf{A}(t_i) | \mathbf{r} | \Psi \rangle, \quad (3)$$

and

$$\mathbf{d}^*[\mathbf{p}(t)] = \langle \Psi | \mathbf{r} | \mathbf{p}_{\text{st}} - \mathbf{A}(t) \rangle. \quad (4)$$

Here Ψ is the ground-state wave function of the target, which is obtained by an *ab initio* calculation in Gaussian software package, and \mathbf{r} denotes the electron coordinate. Then, we calculate the dipole acceleration $\ddot{\mathbf{D}}(t)$ as the second derivative of the time-dependent dipole moment and perform Fourier transform to obtain the harmonic electric field \mathbf{E}_ω in the frequency domain as follows:

$$\mathbf{E}_\omega = \int \ddot{\mathbf{D}}(t) \exp(-i\omega t) dt. \quad (5)$$

To analyze the polarization properties of high-order harmonics, one can decompose the harmonic electric field into two circularly polarized components, namely right- and left-rotating circular polarization. The two circularly polarized components of high-order harmonics can be obtained from their x and y components, and the right- and left-rotating components can be read as

$$\mathbf{E}_\omega^{R/L} = (\mathbf{E}_\omega^x \pm i\mathbf{E}_\omega^y) / \sqrt{2}. \quad (6)$$

The harmonic intensities of the right- and left-rotating components can be obtained by $I_\omega^{R/L} = |\mathbf{E}_\omega^{R/L}|^2$. The degree of circular polarization (DCP) of the high-order harmonics can be calculated as [56]

$$\xi = \frac{I_\omega^R - I_\omega^L}{I_\omega^R + I_\omega^L}. \quad (7)$$

The corresponding harmonic ellipticity ε is connected with the DCP by the formula [56]

$$\varepsilon = \text{sgn}(\xi) \sqrt{\frac{1 - \sqrt{1 - \xi^2}}{1 + \sqrt{1 - \xi^2}}}. \quad (8)$$

In our calculations, the gas mixture consists of Ar atoms and N₂ molecules, each with ground states (the highest occupied orbitals) of $3p$ and $3\sigma_g$, respectively. These highest occupied orbitals exhibit similar ionization energies but possess opposite orbital parities [57,58]. To generate IAPs, we employ a polarization gating laser field composed of two counterrotating circularly polarized laser pulses. The laser field with a time-dependent ellipticity for polarization gating can be resolved into a driving field $\mathbf{E}_x(t)$ and a gating field $\mathbf{E}_y(t)$:

$$\mathbf{E}(t) = \begin{bmatrix} \mathbf{E}_x(t) \\ \mathbf{E}_y(t) \end{bmatrix}. \quad (9)$$

The amplitude E_0 , angular frequency ω_0 , carrier-envelope phase ϕ_0 , and envelope $f(t)$ are the same for the two circularly polarized laser pulses. The driving field along the x direction is

$$\mathbf{E}_x(t) = E_0[f(t) + f(t - \Delta t)] \cos(\omega_0 t + \phi_0) \hat{\mathbf{x}}, \quad (10)$$

and the gating field along the y direction is

$$\mathbf{E}_y(t) = E_0[-f(t) + f(t - \Delta t)] \sin(\omega_0 t + \phi_0) \hat{\mathbf{y}}. \quad (11)$$

$f(t)$ and $f(t - \Delta t)$ represent the envelopes of the left- and right-rotating circularly polarized laser pulses, respectively, in the polarization gating technique, where Δt denotes the time delay between the two pulses. In our calculations, the intensity $I = 1.5 \times 10^{14}$ W/cm², wavelength $\lambda = 800$ nm,

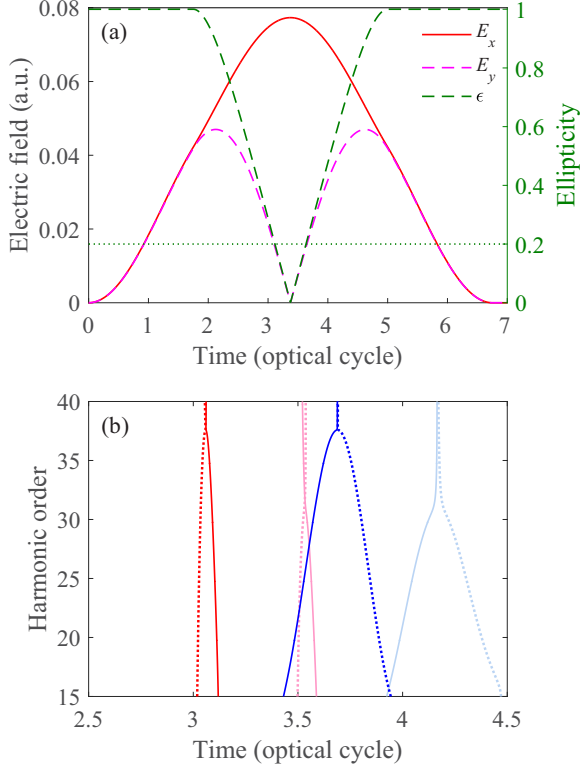


FIG. 1. (a) Amplitudes of the driving field (E_x , red solid line) and gating field (E_y , magenta dashed line) components (left axis). The green dashed line represents the corresponding time-dependent ellipticity (right axis). (b) Calculated the real part of the ionization (red lines) and recombination (blue lines) times for two path pairs. The solid lines correspond to the short paths, and the dashed lines correspond to the long paths.

carrier-envelope phase $\phi_0 = 0$, time delay $\Delta t = 1.75$ optical cycles, and envelope $f(t) = \sin^2(\pi t/T_m)$ with the total duration T_m of five optical cycles for each circularly polarized laser pulse are used. In Fig. 1(a), the amplitudes of the driving field and gating field components are shown as red solid and magenta dashed lines. The time-dependent ellipticity $\epsilon(t) = |f(t) - f(t - \Delta t)| / [f(t) + f(t - \Delta t)]$ is shown as green dashed lines against the right axis [59]. We can see a narrow polarization gate ($\epsilon < 0.2$) between the third and fourth optical cycles, lasting for about half an optical cycle. The driving field generates the attosecond pulse, whereas the gating field suppresses the attosecond pulse emission outside of the polarization gate [60].

To provide a clear description, we explore the behavior of electron paths by solving saddle-point equations [61–64]

$$\frac{[\mathbf{p} + \mathbf{A}(t'_i)]^2}{2} = -I_p, \quad (12)$$

$$\frac{[\mathbf{p} + \mathbf{A}(t'_r)]^2}{2} = \omega - I_p, \quad (13)$$

where ω is the harmonic frequency, $t'_i = t_i + i\text{Im}t'_i$ and $t'_r = t_r + i\text{Im}t'_r$ correspond to the complex times of ionization and recombination, respectively. The real parts t_i and t_r are interpreted as the physical ionization and recombination times. In Fig. 1(b), we present the real ionization times t_i labeled by the

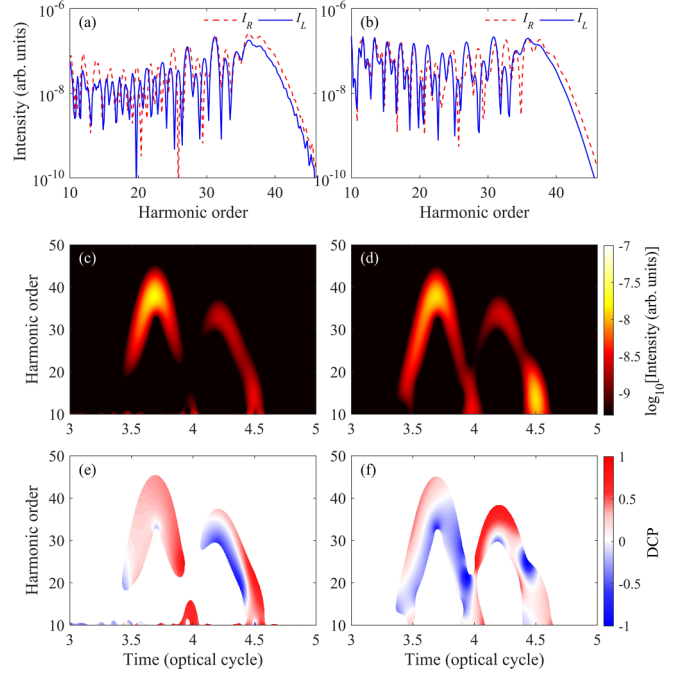


FIG. 2. High-order harmonic spectra for the right- (red dashed lines) and left-rotating (blue solid lines) components from (a) Ar and (b) N₂. The time-frequency distribution of the harmonic intensities from (c) Ar and (d) N₂. The color map represents the time-frequency distribution in the logarithmic scale. The time-frequency distribution of the DCP of high-order harmonics from (e) Ar and (f) N₂.

red lines, as well as the real recombination times t_r labeled by the blue lines. The solid lines are used for the short trajectories and the dashed lines for the long trajectories. There are two recombinations near the polarization gate, resulting in two harmonic radiations (see dark and light blue lines). It can be observed that the cutoff energy of the harmonic radiation before the fourth optical cycle (see dark blue lines) is much higher than that after the fourth optical cycle (see light blue lines) because the maximum kinetic energy of the electron in the first recombination is greater than that in the second one. Only one major emission is chosen in the high-energy region. Therefore, one can superpose the harmonics near the cutoff to generate an IAP. In the following section, we discuss the generation of harmonics and IAPs using the polarization gating technique, as well as the polarization control of the IAPs.

III. RESULTS AND DISCUSSION

Based on the Lewenstein model mentioned in Sec. II, we first calculate the high-order harmonics generated from Ar and N₂, respectively. The harmonic spectra of Ar and N₂ shown in Figs. 2(a) and 2(b) exhibit a supercontinuum in the cutoff region, with comparable right- (red dashed lines) and left-rotating (blue solid lines) components. To elucidate the physics behind the observed supercontinuum and polarization phenomena, we employ the Gabor transform to analyze the time-frequency properties of high-order

harmonics [65]

$$GT(\omega, t) = \int dt' \ddot{D}(t') \frac{\exp[-(t' - t)^2/2\sigma^2]}{\sigma\sqrt{2\pi}} \exp(-i\omega t'), \quad (14)$$

where σ is the width of the Gaussian time window in the Gabor transform, which sets the balance between the resolutions in the temporal and frequency domains [65–67]. In our calculations, we choose $\sigma = 1/3\omega_0$ to achieve an adequate balance between the time and frequency resolutions. The time-frequency distribution of the harmonic intensity is obtained by

$$I_{GT}(\omega, t) = \sum_{j=x,y} |GT_j(\omega, t)|^2. \quad (15)$$

The time-frequency distribution of the DCP is obtained by

$$\xi(\omega, t) = \frac{|GT_R(\omega, t)|^2 - |GT_L(\omega, t)|^2}{|GT_R(\omega, t)|^2 + |GT_L(\omega, t)|^2}, \quad (16)$$

in which $GT_{R/L}(\omega, t) = [GT_x(\omega, t) \pm iGT_y(\omega, t)]/\sqrt{2}$.

The spectrograms in Figs. 2(c) and 2(d) show the time-frequency distribution of harmonic intensities for Ar and N₂. As expected, there are two harmonic radiations, which are consistent with the analysis in Fig. 1(b). The intensity near the cutoff region of the first is notably higher than that of the second. This difference can be attributed to the second being distant from the polarization gate, leading to a decreased probability of electron recombination. Note that the N₂ molecule has an anisotropic spatial structure, and its harmonic efficiency is also influenced by the molecular alignment angle. In the results shown in Fig. 2, the N₂ molecule is aligned at an angle of 60° with respect to the x axis. Compared to the first harmonic radiation, the angle between the electron recollision direction and the molecular axis is smaller in the second harmonic radiation, resulting in the second radiation maintaining considerable intensity. In addition, only once radiation predominates in the high-energy region. The short and long paths gradually converge near the cutoff region. These phenomena result in high-order harmonics displaying a supercontinuum, providing the generation of an IAP. Figures 2(e) and 2(f) show the corresponding time-dependent DCP of high-order harmonics. One can see that, near the cutoff region, the DCP is close to 0, i.e., the intensity of the right-rotating component is nearly equal to that of the left-rotating component. These are directly reflected in Figs. 2(a) and 2(b) where the high-order harmonics are mostly linear when the intense laser field interacts with a single gas for both Ar and N₂. Can elliptically polarized high-order harmonics be generated using the Ar-N₂ mixture? Specifically, is it possible to selectively enhance or suppress a specific polarization component of high-order harmonics through interference effects between harmonics from different gases in the mixture, thereby producing elliptically polarized attosecond pulses? To address this, we perform a quantum orbital analysis of the harmonics generated from a mixture of Ar and N₂.

By substituting the complex times t'_i and t'_r , obtained as solutions of the saddle-point equations [Eqs. (12) and (13)], into Eq. (4), we can determine the recombination dipole moment. The right- and left-rotating components, denoted

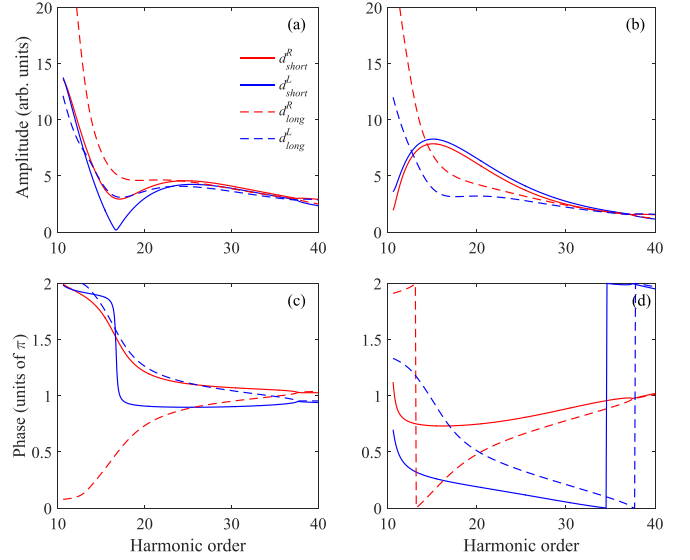


FIG. 3. Amplitudes of the recombination dipole moments for short (solid lines) and long (dashed lines) paths from (a) Ar and (b) N₂. The right-rotating components correspond to red lines, and the left-rotating components correspond to blue lines. The corresponding phases of the recombination dipole moments from (c) Ar and (d) N₂. The alignment angle of N₂ is 60°.

as $\mathbf{d}_k^{R/L}$, are calculated using the formula $(\mathbf{d}_k^x \pm i\mathbf{d}_k^y)/\sqrt{2}$, where $k = s, l$ signifies either the short or long path. The contributions of each path and rotating component to the recombination dipole moment are separately shown in Fig. 3. In Figs. 3(a) and 3(b), it can be seen that the amplitudes of the recombination dipole moments with different helicities, contributed by short (solid lines) or long (dashed lines) path, are almost identical in the high-energy region for both Ar and N₂. Due to the odd parity [i.e. $\Psi_{Ar}(x, y) = -\Psi_{Ar}(-x, -y)$] of the highest occupied orbital 3p, the recombination dipole moments along the x and y directions are purely real values for Ar [68], i.e., $\text{Re}(\mathbf{d}_{Ar}^{x/y}) \neq 0$ and $\text{Im}(\mathbf{d}_{Ar}^{x/y}) = 0$. Consequently, the phases of the recombination dipole moments for the right- and left-rotating components of Ar satisfy the relationship $\tan(\phi_{Ar}^R) = \mathbf{d}_{Ar}^y/\mathbf{d}_{Ar}^x$ and $\tan(\phi_{Ar}^L) = -\mathbf{d}_{Ar}^y/\mathbf{d}_{Ar}^x$, i.e., $\tan(\phi_{Ar}^R) = -\tan(\phi_{Ar}^L)$ in the high-energy region. It can be observed from Fig. 3(c) that the phases ϕ_{Ar}^R (red lines) and ϕ_{Ar}^L (blue lines) are symmetric about π . Furthermore, due to the monoatomic structure of Ar, under the driving of near-linearly polarized laser field within the polarization gate, $\mathbf{d}_{Ar}^y \ll \mathbf{d}_{Ar}^x$, both ϕ_{Ar}^R and ϕ_{Ar}^L are close to π . In contrast, the highest occupied molecular orbital 3 σ_g of N₂ exhibits even parity [i.e., $\Psi_{N_2}(x, y) = \Psi_{N_2}(-x, -y)$], resulting in the recombination dipole moments along the x and y directions being purely imaginary values for N₂ [68], i.e., $\text{Re}(\mathbf{d}_{N_2}^{x/y}) = 0$ and $\text{Im}(\mathbf{d}_{N_2}^{x/y}) \neq 0$. Thus, the phases of the recombination dipole moments for the right- and left-rotating components of N₂ satisfy the relationship $\tan(\phi_{N_2}^R) = -\mathbf{d}_{N_2}^x/\mathbf{d}_{N_2}^y$ and $\tan(\phi_{N_2}^L) = \mathbf{d}_{N_2}^x/\mathbf{d}_{N_2}^y$, i.e., $\tan(\phi_{N_2}^R) = -\tan(\phi_{N_2}^L)$ in the high-energy region. As shown in Fig. 3(d), the phases $\phi_{N_2}^R$ (red lines) and $\phi_{N_2}^L$ (blue lines) are symmetric about $\pi/2$. Additionally, the phase $\phi_{N_2}^R$ mainly distributes between $\pi/2$ and π , while the phase

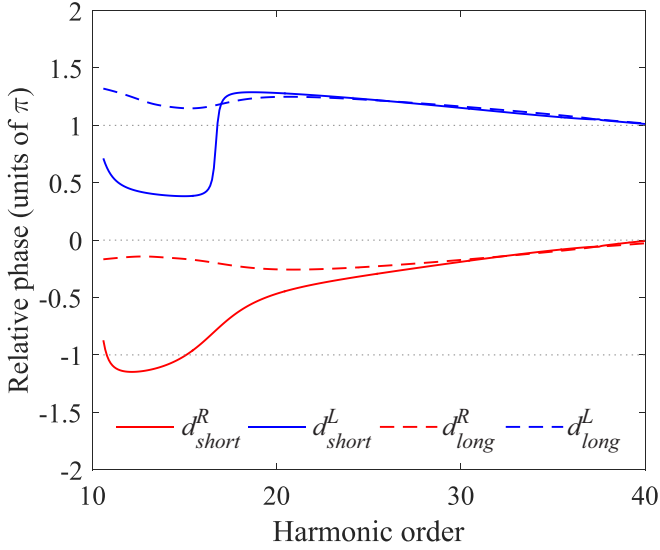


FIG. 4. The relative phases of the recombination dipole moments between Ar and N₂ for short (solid lines) and long (dashed lines) paths. The right-rotating components correspond to red lines, and the left-rotating components correspond to blue lines.

$\phi_{N_2}^L$ between 0 and $\pi/2$. According to the aforementioned results and analysis, the phase difference of the right-rotating components $\Delta\phi_{N_2-Ar}^R$ between N₂ and Ar falls within the range of $[-\pi/2, 0]$, as depicted by the red lines in Fig. 4, whereas the phase difference of the left-rotating components $\Delta\phi_{N_2-Ar}^L$ falls within the range of $[\pi, 3\pi/2]$, as depicted by the blue lines in Fig. 4. For the high-energy region near the cutoff, the phase difference of the right-rotating components is close to 0, and that of the left-rotating components is close to π . The results of short (see solid lines in Fig. 4) and long (see dashed lines in Fig. 4) paths are the same. The highest occupied orbitals of Ar and N₂ have nearly the same ionization potential, thus the phase difference of high-order harmonics radiated from different gas components is primarily attributed to the recombination dipole moments [69].

The intensity of high-order harmonics from mixed gases is the coherent sum of the high-order harmonics from both species. Considering a mixture of Ar and N₂, the total intensity of high-order harmonics with the frequency ω can be calculated by [70,71]

$$I_{\text{mix}}(\omega, \theta) = |\eta E_{Ar}(\omega) \exp[i\varphi_{Ar}(\omega)] + (1 - \eta) \times E_{N_2}(\omega, \theta) \exp[i\varphi_{N_2}(\omega, \theta)]|^2 \\ = \eta^2 E_{Ar}^2(\omega) + (1 - \eta)^2 E_{N_2}^2(\omega, \theta) + 2\eta(1 - \eta) \times E_{Ar}(\omega) E_{N_2}(\omega, \theta) \cos[\Delta\varphi_{N_2-Ar}(\omega, \theta)], \quad (17)$$

where E_{Ar} , E_{N_2} , and φ_{Ar} , φ_{N_2} are the amplitudes and phases of high-order harmonics from Ar and N₂, respectively. η and $1 - \eta$ are the percentages of the two gases in the mixed gases, respectively. In the simulation, we select the percentage η to balance the contributions from two gases in the mixture, ensuring that the amplitudes of high-order harmonics from both gases are evenly matched, thus resulting in pronounced interference. θ is the alignment angle of N₂ respect to the x axis and is set to 60° in the simulation. The

phase difference of high-order harmonics generated from Ar and N₂ primarily arises from the difference in their recombination dipole moments. Therefore, the phase differences of high-order harmonics, denoted as $\Delta\varphi_{N_2-Ar}$, are consistent with the phase differences of their respective recombination dipole moments, $\Delta\phi_{N_2-Ar}$. Specifically, the phase difference of the right-rotating harmonic components from Ar and N₂, $\Delta\varphi_{N_2-Ar}^R$, tends towards 0 near the cutoff region, while that of the left-rotating components, $\Delta\varphi_{N_2-Ar}^L$, tends towards π . In Eq. (17), $\cos[\Delta\varphi_{N_2-Ar}^R(\omega, \theta)]$ is nearly equal to 1, resulting in constructive interference for the right-rotating harmonic components; $\cos[\Delta\varphi_{N_2-Ar}^L(\omega, \theta)]$ is close to -1 , leading to destructive interference for the left-rotating components. Figure 5(a1) shows the spectra of the right- (red dashed line) and left-rotating (blue solid line) harmonic components generated from the mixed gases. The spectra exhibit two distinct characteristics due to the different interference phenomena. For the right-rotating component, we observe a significant enhancement of the supercontinuum. Conversely, for the left-rotating component, we observe a significant weakening. In the plateau region, the intensity of the right-rotating harmonic component is more than one order of magnitude higher than that of the left-rotating component. Near the cutoff region [presented by dotted lines in Fig. 5(a1)], the intensity difference increases to as much as two orders of magnitude, resulting in an overwhelming preference for the right-rotating component.

To quantitatively characterize the polarization of high-order harmonics generated in the mixed gases, we computed the DCP of these harmonics, as illustrated in Fig. 5(b1). It is evident that the DCP above the 34th order is nearly equal to 1 and is consistently right-rotating (with positive values), thereby enabling the synthesis of highly elliptically polarized attosecond pulses. The electric field of the output attosecond pulse synthesized by the high-order harmonics between $[\omega_1, \omega_2]$ could be calculated by an inverse Fourier transform of the spectrum as follows:

$$\mathbf{E}_p(t) = \int_{\omega_1}^{\omega_2} \mathbf{E}_\omega \exp(i\omega t) d\omega. \quad (18)$$

In Fig. 5(c1), we show the projections in the three directions as well as the complete three-dimensional attosecond pulse electric field synthesized from the 34th- to 45th-order harmonics. This synthesized electric field in the time domain directly confirms the elliptical polarization of the attosecond pulse. We estimate the ellipticity of the generated attosecond pulse by calculating the ratio of the minor axis to the major axis of the projection in the x - y plane, which is about 0.86. The intensity of the attosecond pulse, $I_p(t) = |\mathbf{E}_p(t)|^2$, is presented in Fig. 5(d1). It can be seen that there is only one attosecond pulse in the time domain. The full width at half maximum (FWHM) of the IAP is around 290 as. When experimenting with our method, it is crucial to carefully assess the impact of the percentages of the two gases in the mixed gases. Furthermore, we calculate the variation in results as η changes within a range of $\pm 5\%$. The results suggest a slight influence on the ellipticity. As mentioned earlier, we validated our method by solving the two-dimensional TDSE. In the TDSE calculation, N₂ and Ar are modeled using the effective potential

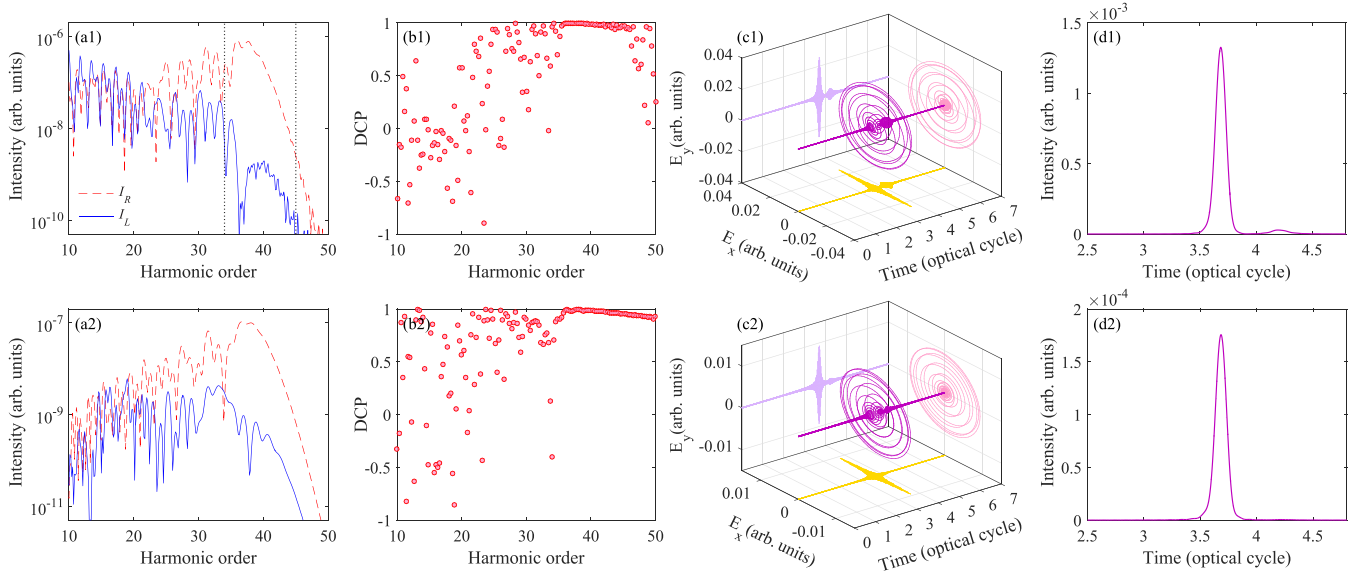


FIG. 5. Results from Ar- N_2 mixed gases based on the Lewenstein model (a1)–(d1) and the TDSE (a2)–(d2). (a1) and (a2) High-order harmonic spectra for the right- (red dashed line) and left-rotating (blue solid line) components, respectively. (b1) and (b2) The DCP of high-order harmonics. (c1) and (c2) Three-dimensional plot of the electric field for the synthesized IAP. (d1) and (d2) Temporal profile of the IAP.

to ensure that the obtained initial states match the parity and ionization potential of their highest occupied orbitals [72–74]. As shown in Fig. 5, the results of the calculation with TDSE [see Figs. 5(a2) to 5(d2)] are shown to be in good agreement with that of the Lewenstein model [Figs. 5(a1) to 5(d1)]. It is worth noting that N_2 is a diatomic molecule with its highest occupied molecular orbital being the $3\sigma_g$ orbital. The high-order harmonics radiated from N_2 depend on the angle between the molecular axis and the polarization of the laser field [70]. By adjusting the molecular alignment angle, the phase difference of the high-order harmonics radiated from Ar and N_2 varies accordingly. As a result, the polarization state of the total high-order harmonics and attosecond pulses can be controlled. Figure 6(a) shows the DCP of the tenth- to 50th-order harmonics as a function of the alignment angle of N_2 in the mixed gases. One can see that as the alignment angle of N_2 is adjusted from 0° to 180° , the DCP of the high-order harmonics produced in the mixed gases initially increases from near 0, and reaches a maximum close to 1 at the alignment angle of 65° . It then gradually decreases to 0, transitions into negative values, and eventually returns to around 0. This depends on the phase difference between the harmonics of N_2 and Ar as the alignment angle changes. When the N_2 is aligned at 65° , the left-rotating component experiences destructive interference, and the right-rotating component experiences constructive interference. This maximizes the intensity difference between the two components, resulting in the maximum DCP. When adjusting the molecular alignment angles, the DCP of high-order harmonics near the cutoff region consistently undergoes synchronous evolution. By utilizing this polarization property of the high-order harmonics generated in mixed gases, the polarization of the synthesized IAPs can be effectively controlled. In Fig. 6(b), we plot the ellipticity of the IAPs synthesized using the high-order harmonics from mixed gases at various alignment angles

for N_2 . Here, the red and blue circles denote right- and left-rotating polarization, respectively. By adjusting the alignment angle of N_2 in the mixed gases, one can continuously vary the ellipticities of IAPs between -0.46 and 0.91 . Importantly, the pulse duration of these IAPs remains constant (not shown), solely determined by the waveform of the laser field.

To effectively generate IAPs, the waveform of the laser field is crucial. In this work, we utilize a polarization gating laser field whose ellipticity varies from circular to linear and then back to circular within a laser pulse envelope. Only the near-linearly polarized portion produces harmonics. In other words, IAPs are selectively generated within a narrow subcycle time window. This method allows for fine-tuned control over the attosecond pulse generation process. Consequently, the temporal profile and intensity of the attosecond pulses are influenced by the CEP of the laser field, which plays a critical role in determining their temporal features and intensity [60]. Figure 7(a) shows the CEP-dependent temporal profile of the attosecond pulses, which are generated from the supercontinuum by the polarization gating laser field. Notably, IAPs can be produced in a wide range of CEP values, with their intensity varying as the CEP changes. At certain CEP values, two attosecond pulses with comparable intensities may appear, although their overall intensities are much weaker. In contrast, as depicted in Fig. 7(b), the DCP of high-order harmonics near the cutoff region remains nearly constant regardless of the CEP variation, except for some CEP values that produce two attosecond pulses. When the CEP ranges from 0 to 0.5π or from π to 1.5π , two harmonic radiations with nearly the same cutoff energy produce two weak attosecond pulses. The interference between these radiations creates a series of minima where the corresponding DCP is close to 0. However, the DCP of the harmonics at nonminima consistently holds the value near 1, ensuring the generation of attosecond pulses with high ellipticity. The information presented in Figs. 6 and 7

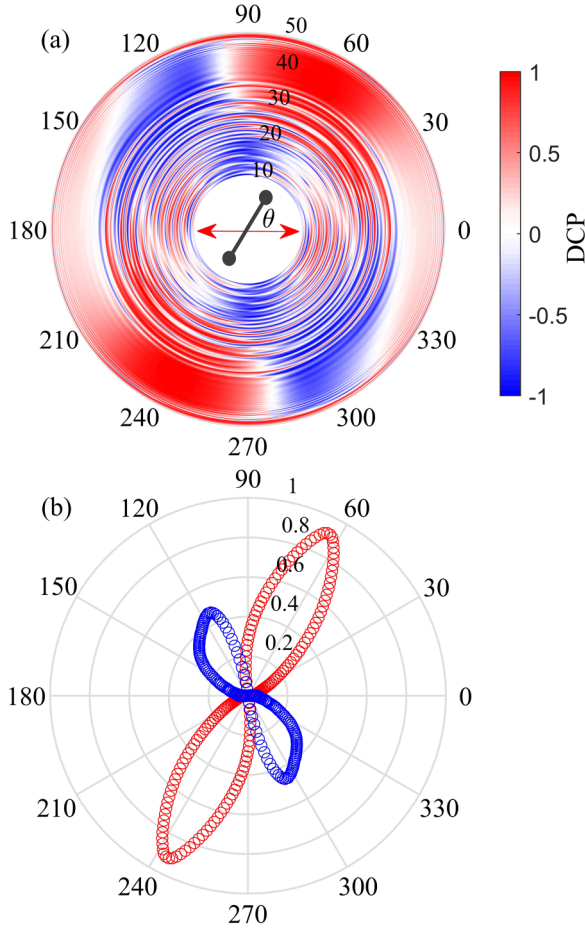


FIG. 6. (a) Polar plot of the DCP of high-order harmonics as a function of harmonic order and the angle between the molecular axis and the x axis. (b) Polar plot of the ellipticity of the IAPs as a function of the angle between the molecular axis and the x -axis. Red indicates positive values and blue negative values.

suggest that the polarization of attosecond pulses is influenced by mixed gases, while their temporal profile is dictated by the waveform of the laser field. Therefore, adjusting the alignment angle of molecules in mixed gases allows us to control the polarization properties of attosecond pulses without impacting their temporal properties. Simultaneously, with the laser field, we can control the temporal properties of attosecond pulses without affecting their polarization properties.

IV. CONCLUSION

In summary, we theoretically investigated the polarization properties of the IAPs generated from mixed gases driven by a gating laser field. By leveraging the advantages of both the mixed gases and the gating field, we can produce near-circularly polarized IAPs in a mixture of Ar and N₂ with a polarization gating laser field. Our numerical results and

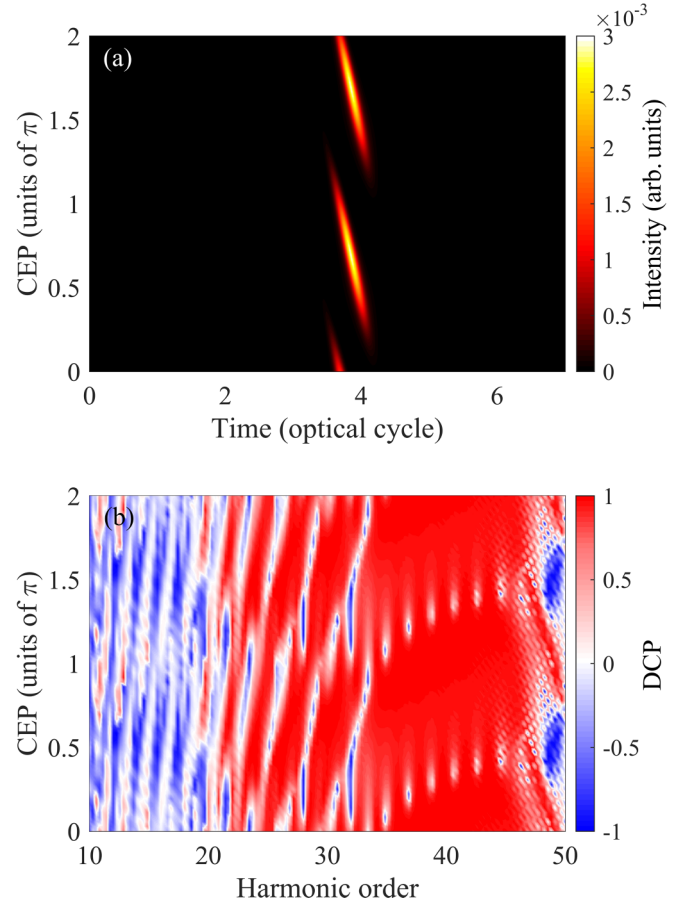


FIG. 7. (a) The dependence of the temporal profile of attosecond pulses on the CEP of the polarization gating laser field. (b) The DCP distribution of harmonics varies with the harmonic order and the CEP.

analyses reveal that different phase differences between the recombination dipole moments of Ar and aligned N₂ for right- and left-rotating components can lead to selective interference. With a given alignment angle, we can selectively enhance one rotating component and weaken the other, thus generating elliptically polarized high-order harmonics with identical helicity. Consequently, we synthesize an IAP with an ellipticity of 0.91 and a duration of 290 as. Further analysis demonstrates that the temporal properties are dependent on the laser field, while the polarization properties on the mixed gases. Our approach provides an effective method for generating elliptical attosecond pulses and enables independent control over both their temporal profile and polarization.

ACKNOWLEDGMENTS

This work was supported by the National Natural Science Foundation of China (Grants No. 12104389, No. 12074329, and No. 12174134) and the Nanhu Scholars Program for Young Scholars of XYNU.

- [1] P. B. Corkum and F. Krausz, *Nat. Phys.* **3**, 381 (2007).
 [2] F. Krausz and M. Ivanov, *Rev. Mod. Phys.* **81**, 163 (2009).

- [3] T. T. Luu, Z. Yin, A. Jain, T. Gaumnitz, Y. Pertot, J. Ma, and H. J. Wörner, *Nat. Commun.* **9**, 3723 (2018).

- [4] S. Ghimire, A. D. DiChiara, E. Sistrunk, P. Agostini, L. F. DiMauro, and D. A. Reis, *Nat. Phys.* **7**, 138 (2011).
- [5] O. D. Mücke, *Phys. Rev. B* **84**, 081202(R) (2011).
- [6] L. Li, P. Lan, X. Zhu, and P. Lu, *Rep. Prog. Phys.* **86**, 116401 (2023).
- [7] R. R. Alfano, S. F. B. Mazhar, and L. Shi, *Optik* **247**, 167872 (2021).
- [8] P. B. Corkum, *Phys. Rev. Lett.* **71**, 1994 (1993).
- [9] M. Nisoli, P. Decleva, F. Calegari, A. Palacios, and F. Martín, *Chem. Rev.* **117**, 10760 (2017).
- [10] R. Borrego-Varillas, M. Lucchini, and M. Nisoli, *Rep. Prog. Phys.* **85**, 066401 (2022).
- [11] L. He, S. Sun, P. Lan, Y. He, B. Wang, P. Wang, X. Zhu, L. Li, W. Cao, P. Lu, and C. D. Lin, *Nat. Commun.* **13**, 4595 (2022).
- [12] L. He, Y. He, S. Sun, E. Goetz, A. T. Le, X. Zhu, P. Lan, P. Lu, and C. D. Lin, *Adv. Photonics* **5**, 056001 (2023).
- [13] A. D. Bandrauk, J. Guo, and K.-J. Yuan, *J. Opt.* **19**, 124016 (2017).
- [14] A. Ferré, C. Handschin, M. Dumergue, F. Burgy, A. Comby, D. Descamps, B. Fabre, G. A. Garcia, R. Géneaux, L. Merceron, E. Mével, L. Nahon, S. Petit, B. Pons, D. Staedter, S. Weber, T. Ruchon, V. Blanchet, and Y. Mairesse, *Nat. Photon.* **9**, 93 (2015).
- [15] D. Baykusheva and H. J. Wörner, *Phys. Rev. X* **8**, 031060 (2018).
- [16] P. Antoine, B. Carré, A. L'Huillier, and M. Lewenstein, *Phys. Rev. A* **55**, 1314 (1997).
- [17] K. S. Budil, P. Salières, A. L'Huillier, T. Ditmire, and M. D. Perry, *Phys. Rev. A* **48**, R3437 (1993).
- [18] P. Dietrich, N. H. Burnett, M. Ivanov, and P. B. Corkum, *Phys. Rev. A* **50**, R3585 (1994).
- [19] N. H. Burnett, C. Kan, and P. B. Corkum, *Phys. Rev. A* **51**, R3418 (1995).
- [20] B. Vodungbo, A. B. Sardinha, J. Gautier, G. Lambert, C. Valentin, M. Lozano, G. Iaquaniello, F. Delmotte, S. Sebban, J. Lüning, and P. Zeitoun, *Opt. Express* **19**, 4346 (2011).
- [21] H. Höchst, R. Patel, and F. Middleton, *Nucl. Instrum. Methods Phys. Res., Sect. A* **347**, 107 (1994).
- [22] D. Azoury, O. Kneller, M. Krüger, B. D. Bruner, O. Cohen, Y. Mairesse, and N. Dudovich, *Nat. Photon.* **13**, 198 (2019).
- [23] J. Levesque, Y. Mairesse, N. Dudovich, H. Pépin, J.-C. Kieffer, P. B. Corkum, and D. M. Villeneuve, *Phys. Rev. Lett.* **99**, 243001 (2007).
- [24] X. Zhou, R. Lock, N. Wagner, W. Li, H. C. Kapteyn, and M. M. Murnane, *Phys. Rev. Lett.* **102**, 073902 (2009).
- [25] X. Xie, A. Scrinzi, M. Wickenhauser, A. Baltuška, I. Barth, and M. Kitzler, *Phys. Rev. Lett.* **101**, 033901 (2008).
- [26] X. Zhang, X. Zhu, X. Liu, F. Wang, M. Qin, Q. Liao, and P. Lu, *Phys. Rev. A* **102**, 033103 (2020).
- [27] N. Saito, P. Xia, F. Lu, T. Kanai, J. Itatani, and N. Ishii, *Optica* **4**, 1333 (2017).
- [28] N. Rana, M. S. Mrudul, and G. Dixit, *Phys. Rev. Appl.* **18**, 064049 (2022).
- [29] Y.-L. He, J. Guo, F.-Y. Gao, and X.-S. Liu, *Phys. Rev. B* **105**, 024305 (2022).
- [30] H. Eichmann, A. Egbert, S. Nolte, C. Momma, B. Wellegehausen, W. Becker, S. Long, and J. K. McIver, *Phys. Rev. A* **51**, R3414 (1995).
- [31] S. Long, W. Becker, and J. K. McIver, *Phys. Rev. A* **52**, 2262 (1995).
- [32] D. B. Milošević and W. Becker, *J. Mod. Opt.* **52**, 233 (2005).
- [33] A. Fleischer, O. Kfir, T. Diskin, P. Sidorenko, and O. Cohen, *Nat. Photon.* **8**, 543 (2014).
- [34] D. B. Milošević, *Opt. Lett.* **40**, 2381 (2015).
- [35] O. Kfir, P. Grychtol, E. Turgut, R. Knut, D. Zusin, D. Popmintchev, T. Popmintchev, H. Nembach, J. M. Shaw, A. Fleischer, H. Kapteyn, M. Murnane, and O. Cohen, *Nat. Photon.* **9**, 99 (2015).
- [36] D. Baykusheva, M. S. Ahsan, N. Lin, and H. J. Wörner, *Phys. Rev. Lett.* **116**, 123001 (2016).
- [37] K. M. Dorney, J. L. Ellis, C. Hernández-García, D. D. Hickstein, C. A. Mancuso, N. Brooks, T. Fan, G. Fan, D. Zusin, C. Gentry, P. Grychtol, H. C. Kapteyn, and M. M. Murnane, *Phys. Rev. Lett.* **119**, 063201 (2017).
- [38] N. Zhavoronkov and M. Ivanov, *Opt. Lett.* **42**, 4720 (2017).
- [39] R. Rajpoot, A. R. Holkundkar, N. Rana, and G. Dixit, *Phys. Lett. A* **493**, 129241 (2024).
- [40] G. Lambert, B. Vodungbo, J. Gautier, B. Mahieu, V. Malka, S. Sebban, P. Zeitoun, J. Lüning, J. Perron, A. Andreev, S. Stremoukhov, F. Ardana-Lamas, A. Dax, C. P. Hauri, A. Sardinha, and M. Fajardo, *Nat. Commun.* **6**, 6167 (2015).
- [41] D. Habibović, W. Becker, and D. B. Milošević, *J. Opt. Soc. Am. B* **38**, 3367 (2021).
- [42] C. Zhai, R. Shao, P. Lan, B. Wang, Y. Zhang, H. Yuan, S. M. Njoroge, L. He, and P. Lu, *Phys. Rev. A* **101**, 053407 (2020).
- [43] Y. Fang and Y. Liu, *Phys. Rev. A* **103**, 033116 (2021).
- [44] D. B. Milošević and D. Habibović, *Phys. Chem. Chem. Phys.* **25**, 28848 (2023).
- [45] D. D. Hickstein, F. J. Dollar, P. Grychtol, J. L. Ellis, R. Knut, C. Hernández-García, D. Zusin, C. Gentry, J. M. Shaw, T. Fan, K. M. Dorney, A. Becker, A. Jaroń-Becker, H. C. Kapteyn, M. M. Murnane, and C. G. Durfee, *Nat. Photon.* **9**, 743 (2015).
- [46] J. L. Ellis, K. M. Dorney, D. D. Hickstein, N. J. Brooks, C. Gentry, C. Hernández-García, D. Zusin, J. M. Shaw, Q. L. Nguyen, C. A. Mancuso, G. S. M. Jansen, S. Witte, H. C. Kapteyn, and M. M. Murnane, *Optica* **5**, 479 (2018).
- [47] P.-C. Huang, C. Hernández-García, J.-T. Huang, P.-Y. Huang, C.-H. Lu, L. Rego, D. D. Hickstein, J. L. Ellis, A. Jaron-Becker, A. Becker, S.-D. Yang, C. G. Durfee, L. Plaja, H. C. Kapteyn, M. M. Murnane, A. H. Kung, and M.-C. Chen, *Nat. Photon.* **12**, 349 (2018).
- [48] K.-Y. Chang, L.-C. Huang, K. Asaga, M.-S. Tsai, L. Rego, P.-C. Huang, H. Mashiko, K. Oguri, C. Hernández-García, and M.-C. Chen, *Optica* **8**, 484 (2021).
- [49] M. Han, J.-B. Ji, K. Ueda, and H. J. Wörner, *Optica* **10**, 1044 (2023).
- [50] M. Hentschel, R. Kienberger, C. Spielmann, G. A. Reider, N. Milosevic, T. Brabec, P. Corkum, U. Heinzmann, M. Drescher, and F. Krausz, *Nature (London)* **414**, 509 (2001).
- [51] G. Sansone, E. Benedetti, F. Calegari, C. Vozzi, L. Avaldi, R. Flammini, L. Poletto, P. Villoresi, C. Altucci, R. Velotta, S. Stagira, S. D. Silvestri, and M. Nisoli, *Science* **314**, 443 (2006).
- [52] K. Zhao, Q. Zhang, M. Chini, Y. Wu, X. Wang, and Z. Chang, *Opt. Lett.* **37**, 3891 (2012).
- [53] J. Li, X. Ren, Y. Yin, K. Zhao, A. Chew, Y. Cheng, E. Cunningham, Y. Wang, S. Hu, Y. Wu, M. Chini, and Z. Chang, *Nat. Commun.* **8**, 186 (2017).
- [54] T. Gaumnitz, A. Jain, Y. Pertot, M. Huppert, I. Jordan, F. Ardana-Lamas, and H. J. Wörner, *Opt. Express* **25**, 27506 (2017).

- [55] M. Lewenstein, P. Balcou, M. Y. Ivanov, A. L'Huillier, and P. B. Corkum, *Phys. Rev. A* **49**, 2117 (1994).
- [56] D. B. Milošević, W. Becker, and R. Kopold, *Phys. Rev. A* **61**, 063403 (2000).
- [57] C. Zhai, X. Zhu, J. Long, R. Shao, Y. Zhang, L. He, Q. Tang, Y. Li, P. Lan, B. Yu, and P. Lu, *Phys. Rev. A* **103**, 033114 (2021).
- [58] C. Zhai, Y. Wu, X. Li, K. Zhang, S. Kang, Z. Li, F. Guo, Y. Li, Q. Tang, and B. Yu, *J. Phys. B: At. Mol. Opt. Phys.* **56**, 195601 (2023).
- [59] Z. Chang, *Phys. Rev. A* **70**, 043802 (2004).
- [60] A. R. Madhani, E. Irani, and M. Monfared, *Opt. Express* **31**, 18430 (2023).
- [61] P. Salières, B. Carré, L. L. Déroff, F. Grasbon, G. G. Paulus, H. Walther, R. Kopold, W. Becker, D. B. Milošević, A. Sanpera, and M. Lewenstein, *Science* **292**, 902 (2001).
- [62] D. Shafir, H. Soifer, B. D. Bruner, M. Dagan, Y. Mairesse, S. Patchkovskii, M. Y. Ivanov, O. Smirnova, and N. Dudovich, *Nature (London)* **485**, 343 (2012).
- [63] D. Baykusheva, S. Brennecke, M. Lein, and H. J. Wörner, *Phys. Rev. Lett.* **119**, 203201 (2017).
- [64] R. Shao, C. Zhai, Y. Zhang, N. Sun, W. Cao, P. Lan, and P. Lu, *Opt. Express* **28**, 15874 (2020).
- [65] C. C. Chirilă, I. Dreisigacker, E. V. van der Zwan, and M. Lein, *Phys. Rev. A* **81**, 033412 (2010).
- [66] N. Rana, M. S. Mrudul, and G. Dixit, *Phys. Rev. B* **110**, 054103 (2024).
- [67] I. N. Ansari, M. S. Mrudul, M. F. Ciappina, M. Lewenstein, and G. Dixit, *Phys. Rev. A* **98**, 063406 (2018).
- [68] S. Haessler, J. Caillat, W. Boutu, C. Giovanetti-Teixeira, T. Ruchon, T. Auguste, Z. Diveki, P. Breger, A. Maquet, B. Carré, R. Taïeb, and P. Salières, *Nat. Phys.* **6**, 200 (2010).
- [69] A. Camper, A. Ferré, V. Blanchet, D. Descamps, N. Lin, S. Petit, R. Lucchese, P. Salières, T. Ruchon, and Y. Mairesse, *Phys. Rev. Lett.* **130**, 083201 (2023).
- [70] J. B. Bertrand, H. J. Wörner, P. Salières, D. M. Villeneuve, and P. B. Corkum, *Nat. Phys.* **9**, 174 (2013).
- [71] C. Zhai, Y. Wu, Y. Liu, K. Zhang, S. Kang, Z. Li, F. Wu, X. Dong, X. Cheng, Y. Li, Q. Tang, and B. Yu, *Results Phys.* **58**, 107518 (2024).
- [72] M. Peters, T. T. Nguyen-Dang, E. Charron, A. Keller, and O. Atabek, *Phys. Rev. A* **85**, 053417 (2012).
- [73] X. Zhu, X. Liu, Y. Li, M. Qin, Q. Zhang, P. Lan, and P. Lu, *Phys. Rev. A* **91**, 043418 (2015).
- [74] I. Barth and M. Lein, *J. Phys. B: At. Mol. Opt. Phys.* **47**, 204016 (2014).